remote sensing

MDPI

Article

Meteorological Drivers of Permian Basin Methane Anomalies Derived from TROPOMI

Erik Crosman

Department of Life, Earth and Environmental Sciences, West Texas A&M University, Canyon, TX 79016, USA; etcrosman@wtamu.edu

Abstract: The launch of the TROPOspheric Monitoring Instrument (TROPOMI) on the Sentinel-5 Precursor (S-5P) satellite has revolutionized pollution observations from space. The purpose of this study was to link spatiotemporal variations in TROPOMI methane (CH_4) columns to meteorological flow patterns over the Permian Basin, the largest oil and second-largest natural gas producing region in the United States. Over a two-year period (1 December 2018–1 December 2020), the largest average CH_4 enhancements were observed near and to the north and west of the primary emission regions. Four case study periods—two with moderate westerly winds associated with passing weather disturbances (8–15 March 2019 and 1 April–10 May 2019) and two other periods dominated by high pressure and low wind speeds (16–23 March 2019 and 24 September–9 October 2020)—were analyzed to better understand meteorological drivers of the variability in CH_4. Meteorological observations and analyses combined with TROPOMI observations suggest that weakened transport out of the Basin during low wind speed periods contributes to CH_4 enhancements throughout the Basin, while valley and slope flows may explain the observed western expansion of the Permian Basin CH_4 anomaly.

Keywords: CH_4; NO_2; TROPOMI; remote sensing; air quality; oil and natural gas emissions; Permian Basin; pollution transport; boundary-layer flows

Citation: Crosman, E. Meteorological Drivers of Permian Basin Methane Anomalies Derived from TROPOMI. *Remote Sens.* **2021**, *13*, 896. https://doi.org/10.3390/rs13050896

Academic Editor: Hyung Joo Lee

Received: 29 December 2020
Accepted: 24 February 2021
Published: 27 February 2021

1. Introduction

The rapid growth in horizontal drilling and hydraulic fracturing in oil and natural gas (ONG) production regions over the past 20 years has implications for water quality, air quality, and climate [1–8]. Two important trace gas emissions resulting from ONG production are nitrogen dioxide (NO_2) and methane (CH_4). NO_2 impacts respiratory and cardiovascular health and is a precursor pollutant for secondary pollutants such as ozone [9,10]. As a greenhouse gas, CH_4 is more potent than carbon dioxide (CO_2), such that, as CH_4 emissions increase through ONG production, its positive benefits as a cleaner burning fuel can be overshadowed by its climate forcing [11,12]. Consequently, there has been considerable research on improving understanding of highly variable emissions of CH_4 and other trace gases from ONG production regions [13–18].

The Permian Basin of West Texas and southeastern New Mexico (Figure 1) covers approximately 160,000 square kilometers and is the largest oil producing region and second-largest natural gas producing region in the USA [15]. Since 2007, the Permian Basin crude oil production has quadrupled, while natural gas production has more than doubled [15]. The Permian Basin is composed of two major clusters of ONG drilling and extraction activity, the Delaware Basin on the western side of the Basin and the Midland Basin to the east (not shown). The Midland Basin is dominated by oil extraction, while both oil and natural gas extraction activities are focused in the Delaware Basin. While ONG production occurs throughout the Basin, the most active regions of combined ONG production are located in the center of the Basin (Figure 1) [19]. A recent study found decreases in CH_4 emissions associated with declines in ONG activity during the COVID-19 pandemic [19], while another study found that CH_4 emissions estimates from ground-based observations in the Permian Basin were 5.5–9.0 times greater than EPA National Inventory Estimates [15].

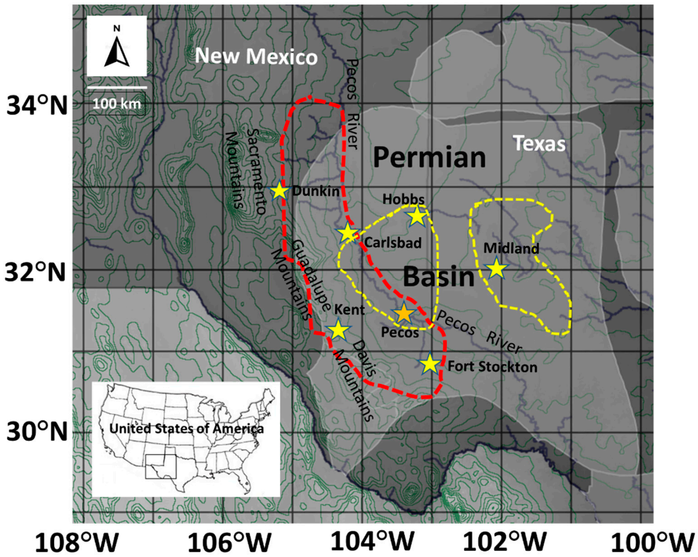

Figure 1. A map of the Permian Basin (labeled shaded grey region), including states (named in white text), mountain ranges, and the Pecos River basin. Topographical contours are shown each 150 m and map elevation ranges from near 400 m near the southeastern corner of the basin to over 2500 m in the highest elevations of the Sacramento, Guadalupe, and Davis Mountains. Yellow stars indicate the location of six weather observation sites analyzed in this study (Table 1). The orange star denotes Pecos, Texas where transport model trajectories were initialized. The approximate regions of the most concentrated oil and natural gas production are outlined in yellow based on a production heatmap [19], whereas the region denoted in red encompasses the approximate location of the western Permian Basin where terrain-driven transport processes may contribute to a western expansion of the Permian Basin CH_4 anomaly.

Table 1. Meteorological Surface Stations.

Station Name	Network	Elevation (m)	Latitude °N/Longitude °W
Fort Stockton	TEXAS ASOS	917	30.91194/102.91667
Kent 9E	TEXAS DCP	1221	31.08859/104.05490
Midland Intl	TEXAS ASOS	869	31.94662/102.20745
Carlsbad	NM ASOS	1004	32.33747/104.26328
Dunken Raws	NM DCP	1647	32.82560/105.18060
Hobbs/Lea Co.	NM ASOS	1115	32.68753/103.21703

Satellite remote sensing of air pollution, including from ONG activities, has been ongoing for several decades [20–22], but has been recently revolutionized by the European Space Agency's Sentinel-5 Precursor (S-5P) polar-orbiting satellite, launched on 13 October 2017 [23–25]. The TROPOspheric Monitoring Instrument (TROPOMI) onboard the S-5P satellite contains four spectrometers that enable accurate, high resolution (temporally and spatially) retrievals for a number of atmospheric constituents (e.g., NO_2, CH_4, carbon monoxide (CO), sulfur dioxide (SO_2), ozone (O_3), and aerosols [23]). The high spatial resolution of TROPOMI measurements has led to recent studies investigating the impacts of meteorological, social, or economic forcing (e.g., COVID-19 pandemic) on the spatial and temporal variability of NO_2 [26–31]. Recent studies across the world (e.g., Europe [32,33], Canada [34], USA [35], and China [36]) have linked changes in NO_2 to meteorological variations (e.g., solar angle and wind speed). In Alberta, Canada, TROPOMI NO_2 observations were validated over plumes from individual mining facilities [37]. CH_4, in contrast, is not reactive on atmospheric transport time scales (CH_4 has lifetime of 8–12 years). Therefore, CH_4 has been used in atmospheric inversion modeling and transport studies to estimate natural and anthropogenic emissions [38,39].

TROPOMI satellite retrievals of NO_2 and CH_4 have been extensively validated over the past several years. TROPOMI tropospheric and total NO_2 column data have been compared against NO_2 spectrometers, with a general negative bias (-23% to -51%) for tropospheric column data attributed to errors in chemical transport models, cloud effects and aerosols [40]. Other studies, comparing aircraft- and ground-based spectrometer measurements in urban and non-urban areas. have also found a systematic underestimation in TROPOMI NO_2 measurements, particularly during highly polluted conditions [34,41–45].

The TROPOMI CH_4 measurements have also been recently validated. Two years of validation of TROPOMI CH_4 measurements against the Total Carbon Column Observing Network (TCCON) showed good agreement between satellite and TCCON data (-3.4 mean bias and ± 5.6 ppbv standard deviation) [46], while other CH_4 measurement validation studies also found generally good agreement between TROPOMI and surface-based measurements [47–49]. In the Uintah Basin ONG producing region, TROPOMI methane columns have been shown to be well correlated with in situ measurements, while the methane columns were also correlated with the Lamont TCONN site in Oklahoma [25]. The retrievals have, however, been found to be sensitive to surface albedo, and a recent correction has been implemented [46].

In this study, spatiotemporal variations in TROPOMI methane (CH_4) and nitrogen dioxide (NO_2) measurements are linked to meteorological flow patterns over the Permian Basin. A recent TROPOMI-derived CH_4 emissions study noted an unexplained CH_4 enhancement northwest of the primary Permian Basin ONG production region [50]. In this study, we combined TROPOMI observations with meteorological observations, analyses, and trajectory simulations to improve understanding of meteorological drivers of CH_4 anomalies in the Permian Basin.

This paper is organized as follows. Section 2 contains the data and methods. The climatological and case study results are presented in Section 3, with a discussion in Section 4. Conclusions and future research recommendations are given in Section 5.

2. Materials and Methods

2.1. TROPOMI Sensor Data and the Google Earth Engine (GEE)

Observations from the TROPOMI sensor on-board the S-5P satellite were used in this study. The S-5P mission, launched by the European Space Agency in 2017, is a polar-orbiting satellite used to monitor Earth's atmosphere with a high spatiotemporal resolution [23]. TROPOMI sensor reflectance measurements in the ultraviolet, visible, near-infrared, and short-wave infrared allow for the retrieval of ozone, methane (CH_4), aerosols, carbon monoxide, nitrogen oxide (NO_2), and sulfur dioxide. The TROPOMI satellite swaths (width 2600 km) are able to cover most of the globe on a daily basis (see Table S1 for pixel resolution). Shortwave infrared spectral radiance measurements are used in the Weighting Function Modified DOAS (WFM-DOAS) algorithm to retrieve $CH_{4.}$ The TROPOMI NO_2 column retrieval algorithms are based on the established DOMINO and QA4ECV processing systems [51,52].

TROPOMI daily offline Level 3 (OFFL L3) CH_4 and NO_2 measurements archived and stored on the Google Earth Engine (GEE) cloud-based platform [53] over the Permian Basin for a two-year period between 1 December 2018 and 1 December 2020 were analyzed in this study (Table 2 and Table S1).

Table 2. TROPOMI sensor Level 3 products from Google Earth Engine (GEE) Cloud Data Archive used in processing the Level 3 GEE products. Refer to Table S1 for information about the underlying L2 TROPOMI products, resolution, and algorithm versions used.

Resolution.	Product	Band Name (Units)
0.01 arc degrees	GEE Sentinel-5P OFFL CH4	Band name: CH4_column_volume_mixing_ratio_dry_air (ppbv)
0.01 arc degrees	GEE Sentinel-5P OFFL NO2	Band name: NO2_column_volume_number_density (mol/m^2)

The GEE is a "cloud-based platform for . . . geospatial analysis that brings Google's massive computational capabilities" to important societal issues [53]. Use of GEE has rapidly increased [54], and it was the focus of a Special Issue of the MDPI journal Remote Sensing [55]. Our analysis of TROPOMI CH_4 and NO_2 observations were processed using the JavaScript editor within the GEE developer framework (the JavaScript code used is available to anyone interested via request from the author). The mean values for the NO_2 and CH_4 data for the period of study, as well as for four case study periods of interest, were calculated.

2.1.1. TROPOMI CH_4 Data

The GEE L3 daily Sentinel-5P OFFL CH4 product [56], band name "CH4_column_volume_mixing_ratio_dry_air", in units of parts per billion by volume (ppbv) between 1 December 2018 and 1 December 2020 was processed through the GEE. Table S1 lists the product versions of the L2 TROPOMI data used in processing the L3 data. Data quality filtering was done through the harpconvert tool with the bin spatial operation [57], which filters and removes pixels with quality assurance flags below 50% to remove cloud contamination and other poor-quality retrievals. Over the two-year period analyzed, the number of available CH_4 columns for each pixel location over the Permian Basin ranged from approximately 50 to 250 for CH_4 (i.e., a valid pixel available on average 7–35% of all days). During the case study periods (Section 3.2), which range from 7 to 40 days in length, the number of available CH_4 observations ranged from 2 to 15 (days) across most of the Permian Basin.

2.1.2. TROPOMI NO_2 Data

The GEE L3 daily Sentinel-5P OFFL NO2 product [58], band name "NO2_column_ volume_number_density", in units of mol/m^2 between 1 December 2018 and 1 December 2020 was processed through the GEE. Table 2 lists the product versions of the L2 TROPOMI data used in processing the L3 data. Data quality filtering was done through the harpconvert tool with the bin spatial operation [57], which filters and removes pixels with quality assurance flags below 75% to remove poor-quality retrievals from the analysis. The TROPOMI NO_2 data had almost daily coverage.

2.2. *Sources of Error*

While both the TROPOMI CH_4 and NO_2 products have been extensively validated (see discussion in the Introduction), there are several important considerations when using these products. Users of the TROPOMI products should carefully read the available Algorithm Theoretical Basis Documents, Product User Manuals, and Readme documents at the TROPOMI website [51] and compare with the available data and product versions on the GEE platform (see Table S1) [56,58]. The GEE platform, while powerful for ease of access and rapid geospatial analysis, does not always include reprocessed data and corrected product versions. The various CH_4 and NO_2 Level 2 product versions used in this study are provided in Table S1.

The TROPOMI CH_4 retrievals have gone through a number of algorithm improvements, including a constant regularization algorithm scheme and higher resolution surface altitude database (Table S1). In addition, the TROPOMI measurements have been found to be highly sensitive for low and high land surface albedo, and a posteriori correction for low and high land surface albedo was implemented [46,47,59] and the corrected product made available (however, the corrected albedo product is not yet available in GEE at the time of this publication [56]).

The TROPOMI NO_2 retrievals have also seen a number of improvements in the algorithm and product versions, including a "destriping" algorithm, quality assurance flag for over snow and ice, and improved cloud retrieval. An important note for anyone using future NO_2 retrievals is that the version implemented on 2 December 2020 (V01.04.00), which includes improved handling of cloud pressure, will result in higher values than earlier versions (offsetting the bias in polluted regions noted in validation studies). Thus, users should not combine V01.04.00 and previous versions to look at NO_2 trends [51,52,60].

Trends and seasonal variations in CH_4 and NO_2 were not calculated for this study due to multiple versions of the satellite products (which could introduce temporal changes resulting from the different product version) available in GEE, as well as not having access to the a posteriori albedo correction for CH_4 data in GEE [46]. In addition, analysis of the temporal availability (not shown) of the CH_4 retrievals indicated that in the cloudier, cooler season there was frequently fewer available data. Spatial differences in the number of valid retrievals were also noted across the region, with several small areas showing no valid pixels over the entire two years. A more detailed analysis of errors introduced by spatial and temporal data gaps is needed before attempting trend and seasonal analyses with TROPOMI CH_4 observations in this region even if consistent and corrected product versions were analyzed.

2.3. Meteorological 10-m Wind Observations and Analysis

Meteorological wind speed (in meters per second, m s^{-1}) and direction data (in degrees) from six near-surface (10-m above ground level (AGL)) weather stations in the region were obtained from Mesowest [61,62], and the Iowa State Mesonet [63]. Wind roses were analyzed with the Iowa State University custom wind rose feature [63].

The location of the surface weather stations that were used for 10-m AGL wind speed and direction analysis for this study are shown in Figure 1. The station name, network organization, location, and elevation are listed in Table 1.

2.4. NCEP/NCAR Reanalyses and NOAA HYSPLIT Model

Meteorological reanalysis data from the National Center for Environmental Prediction (NCEP) and National Center for Atmospheric Research (NCAR) reanalysis product (NCEP/NCAR) of 700 hPa winds and 500 mb heights were obtained from the National Oceanic and Atmospheric Administration (NOAA) Physical Sciences Laboratory [64].

The NOAA HYbrid Single-Particle Lagrangian Integrated Trajectory (HYSPLIT) model [65,66] was run for a 60-h period between 1200 Universal Time Coordinated (UTC) on 30 September 2020 and 0000 UTC on 3 October 2020, with single particle forward trajectories calculated starting at 100 m AGL every 5 h at Carlsbad, New Mexico (see Table 1) and Pecos, Texas (Figure 1). The NOAA High Resolution Rapid Refresh (HRRR) model at 3 km horizontal grid resolution was used at the meteorological input for the HYSPLIT particle trajectory calculations [67].

3. Results

3.1. TROPOMI Mean CH_4 and NO_2 1 December 2018–1 December 2020

The average NO_2 tropospheric column number density (in mol/m^2) over the Permian Basin for the 24-month period from 1 December 2018 to 1 December 2020 is shown in Figure 2.

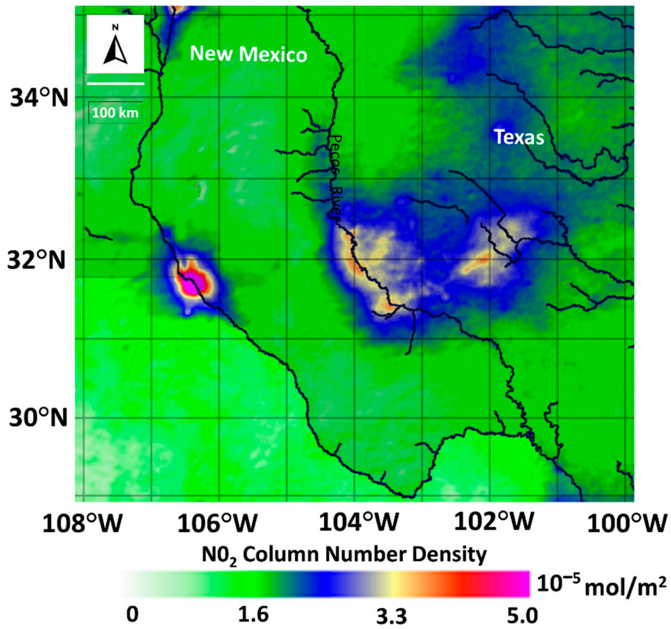

Figure 2. Average TROPOMI nitrogen dioxide tropospheric column number density (NO_2, in mol/m^2) over the Permian Basin region (Figure 1) for the 24-month period 1 December 2018–1 December 2020.

Because NO_2 has a short lifetime (1–12 h depending on the time of year) in the atmosphere before reacting to form secondary pollutants, the highest NO_2 enhancements will be relatively close to emission sources. As discussed in the Introduction, many recent studies have leveraged the high temporal and spatial resolution of TROPOMI to investigate the impacts of meteorological variables on the transport and spatial distribution of NO_2 [26–37].

Due to the complexity of anthropogenic emission sources of NO_2 over the Permian Basin (from ONG infrastructure, numerous small towns, and several larger cities such as Midland and Odessa, Texas), no attempt is made at attributing or describing the source locations from which the observed NO_2 enhancements occurred. The sparsely populated arid regions to the north, south and west of the Permian Basin observe low NO_2 tropospheric column number densities as expected due to a lack of anthropogenic activities. In contrast, the regions with the most ONG production activities in the Permian Basin observe notable NO_2 enhancements compared to the surrounding regions. The highest observed mean NO_2 tropospheric column number densities were found in the Western Delaware Basin extending from near Carlsbad, New Mexico to near Pecos, Texas as well as in a broad region surrounding Midland, Texas (Figure 2). The general spatial patterns observed in the two-year climatological NO_2 plot are similar to the "heat map" plots of density of ONG production in the Basin [19], suggesting that at least a significant portion of the NO_2 observed by TROPOMI across the Basin is associated with ONG production activities.

The average CH_4 column average mixing ratio (in ppbv) over the Permian Basin for the 24-month period extending from 1 December 2018 to 1 December 2020 are shown in Figure 3.

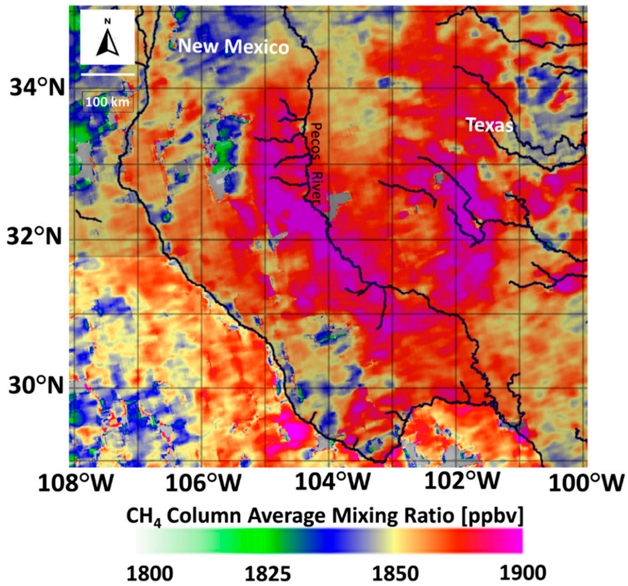

Figure 3. Average TROPOMI CH_4 column average mixing ratio (ppbv) over the Permian Basin region (denoted in Figure 1) for the 24-month period 1 December 2018–1 December 2020.

Because CH_4 has a long lifetime (several years) in the atmosphere and is comprised of both local and background sources, variable CH_4 columns are noted throughout the Permian Basin. In addition, variability (in both space and time) in background CH_4 measurements and trends are noted regionally, so it is not possible without more detailed analysis of background CH_4 measurements combined with local source emission data to quantify the relative magnitude of local versus non-local (background) and anthropogenic versus non-anthropogenic CH_4 from satellite imagery. Finally, because the Playa desert regions to the west of the Permian Basin have high albedo, the CH_4 retrievals shown in Figure 3 in that region are likely biased high based on comparison with a recent study that included albedo corrections [50]. Over the main portion of the Permian Basin, the albedo is in the moderate range (0.15–0.25) [68], so large impacts on the retrievals from either excessively high albedo such as observed over reflective playas or very low albedo such as observed over the northeastern great plains as discussed in [25] are not expected.

The regions with the highest average CH_4 column average mixing ratio (Figure 3) are located in a broad swath encompassing the most dense ONG production regions, but also extending west and northwestward between 50 and 125 km from the western edge of the primary ONG production regions (Figure 3). This region is bounded to the east by the Pecos River Valley and to the west by the eastern slopes of the West Texas and New Mexico mountains (Figure 1). As discussed in Section 3.3, the northwestward transport of CH_4 by upvalley and upslope flows is hypothesized to contribute to the observed western enhancements in TROPOMI CH_4 columns (Figure 1).

3.2. *Case Studies: Meteorological Drivers of Spatial and Temporal Variability of CH_4 and NO_2*

Several interesting spatial patterns have emerged in the average variability of CH_4 columns cross the Permian Basin between 1 December 2018 and 1 December 2020 (Figure 3). In the next two subsections, the impacts of meteorological transport for four case study periods—two with frequent westerly winds (8–15 March 2019 and 1 April–10 May 2019, referred to as the "windy" cases) and two dominated by high pressure and low wind speeds (16–23 March 2019 and 24 September–9 October 2020, referred to as the "quiescent" cases)—are presented.

3.2.1. Short-Duration Meteorological Forcing Case Studies (8 Days)

The mean CH_4 and NO_2 TROPOMI columns over the Permian Basin for two short-duration case studies (8–15 and 16–23 March 2019) are shown in Figure 4, the associated

NCEP/NCAR meteorological analysis are presented in Figure 5, and wind rose analyses of near surface (10 m) wind observations are displayed in Figure S1.

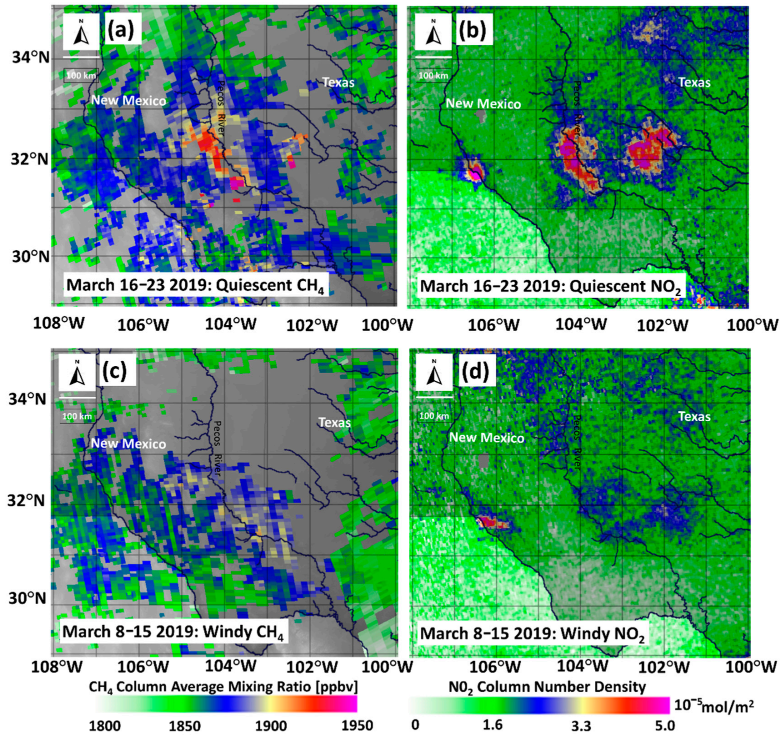

Figure 4. Average TROPOMI CH_4 column average mixing ratio (ppbv) for: (**a**) 16–23 March 2019 (quiescent); and (**c**) 8–15 March 2019 (windy). Average TROPOMI nitrogen dioxide tropospheric column number density (NO_2, in mol/m^2) for: (**b**) 16–23 March 2019 (quiescent); and (**d**) 8–15 March 2019 (windy).

This 16-day consecutive period in March 2019 was chosen because of the back-to-back progression of a strong weather system (Figure 5c,d, a "windy" case) immediately followed by a high amplitude ridge of high pressure aloft (Figure 5a,b, a "quiescent" case). By choosing to evaluate short, consecutively occurring time periods for the two case studies, the impacts of the weather systems on the atmospheric trace gas measurements from TROPOMI can be more easily ascertained because changes in the satellite estimates resulting from variations in seasonal or background trace gas concentrations, or in local trace gas emission trends due to economic or other factors, can be largely ignored over such a short time period. By observing the build-up of trace gases during a mostly quiescent period following a windy period, the impacts of residual trace gas emissions trapped in the boundary-layer during the first case contaminating the satellite retrievals in the second case can also be avoided.

The meteorological conditions across the Permian Basin during the windy short-term case study period (8–15 March 2019) were characterized by the slow passage of a large low pressure system and associated jet stream over the western USA at 500 hPa, while average 700 hPa wind speeds were between 12 and 16 m s^{-1} (Figure 5c,d). At the surface, westerly flow greater than 10 m s^{-1} was noted over much of the eight-day period at Dunkin, on the western slopes of the Sacramento Mountains, while periods of westerly winds over 10 m s^{-1} were frequently noted in the Pecos River Valley (at Carlsbad) (Figure S1). These westerly winds would act to transport any emissions of CH_4 and NO_2 within the Basin to the east and northeast relatively rapidly.

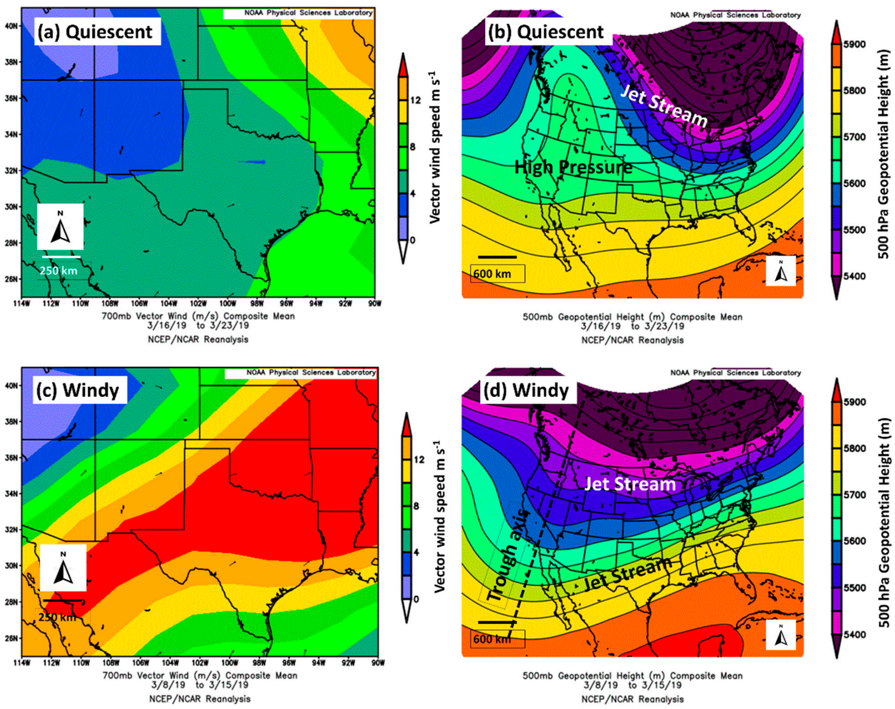

Figure 5. National Centers for Environmental Prediction (NCEP) NCEP/NCAR reanalysis of 700 hPa winds and 500 hPa geopotential heights for: (**a**) 700 hPa winds 16–23 March 2019 (quiescent); (**b**) 500 hPa geopotential heights from 16–23 March 2019 (quiescent); (**c**) 700 hPa winds 8–15 March 2019 (windy); and (**d**) 500 hPa geopotential heights 8–15 March 2019 (windy). Image composites were produced by the National Oceanic and Atmospheric Administration (NOAA) Physical Sciences Laboratory at their website https://www.psl.noaa.gov/data/composites/day/ (accessed on 14 February 2021).

In contrast to the windy period, the meteorological conditions across the Permian Basin during the quiescent (low wind speed) short-duration case study period (16–23 March 2019) were characterized by high pressure across the western USA at 500 hPa and average 700 hPa wind speeds ~5 m s^{-1} over the Permian Basin (Figure 5a,b). These are ~35% of the wind speed noted the week prior (i.e., the "windy" case). At the surface, very weak terrain-driven (upslope and downslope at Dunkin and upvalley and downvalley at Carlsbad) flows were noted, with mean wind speeds only 3.3–3.4 m s^{-1} at these locations (Figure S1). These weak thermally and terrain-driven flows would reduce transport of any emissions of CH_4 and NO_2 within the Permian Basin to regions outside of the Basin during this time period.

Comparing the spatial pattern in TROPOMI NO_2 between the quiescent and windy cases (Figure 4b,d) shows clearly the impact of the increased wind speeds on the retrievals, with a smaller spatial footprint and mean NO_2 column number density observed during the windy case (about half the values of mean NO_2 column number density in the windy case compared to the quiescent conditions). Because the lifetime of NO_2 varies during the seasons, by analyzing two short time periods adjacent to each other, we can see more clearly the impact of variations in large-scale winds and mixing on the satellite NO_2 retrievals without having to account for the impacts of seasonal variations in the lifetime of NO_2. Interestingly, the impact of westerly winds on transporting a thin plume of NO_2 from El Paso, Texas towards to east can also be seen in the mean NO_2 column number density during the windy period (Figure 4d).

Comparing the spatial pattern in TROPOMI CH_4 between the quiescent and windy cases (Figure 4a,c) shows clearly the impact of the increased wind speeds on the retrievals in the primary ONG emissions region around Carlsbad, NM, where the average TROPOMI CH_4 column average mixing ratio values are about 40–50 ppbv higher during the quiescent case than during the windy case, but a lack of pixel values in many parts of the

Basin (valid pixels were only noted on 2–3 days during each eight-day case study period, and these were often in different locations) results in less confidence (or no information) in the values obtained for CH_4 in those regions.

3.2.2. Longer-Term Meteorological Forcing Case Studies

In this section, we analyze mean satellite retrievals of CH_4 alongside meteorological measurements for two longer periods of analysis than in the short-term case studies (16–40 days). The mean CH_4 and NO_2 TROPOMI columns over the Permian Basin for the two longer-term case studies (24 September–9 October 2020, "quiescent" case, and 1 April–10 May 2019, "windy" case) are shown in Figure 6, the associated NCEP/NCAR meteorological analysis are presented in Figure 7, and wind rose analyses of near surface (10 m) wind observations are displayed in Figure S2. Note that these results need to be very carefully evaluated, since, by choosing to analyze a longer time period, the impacts of the weather systems on the atmospheric trace gas measurements from TROPOMI are difficult to ascertain because changes in the satellite estimates resulting from seasonal variations in trace gases, ground emissions, background concentrations, and other factors cannot be avoided. In addition, changes in the algorithm versions (Table S1) and a lack of availability of retrievals also could potentially impact longer averaging periods. However, due to the spotty and infrequent retrievals of CH_4, longer mean calculations for case studies for both windy (1 April–10 May 2019) and quiescent (24 September–9 October 2020) cases are still evaluated in this section, keeping the limitations of this approach in mind.

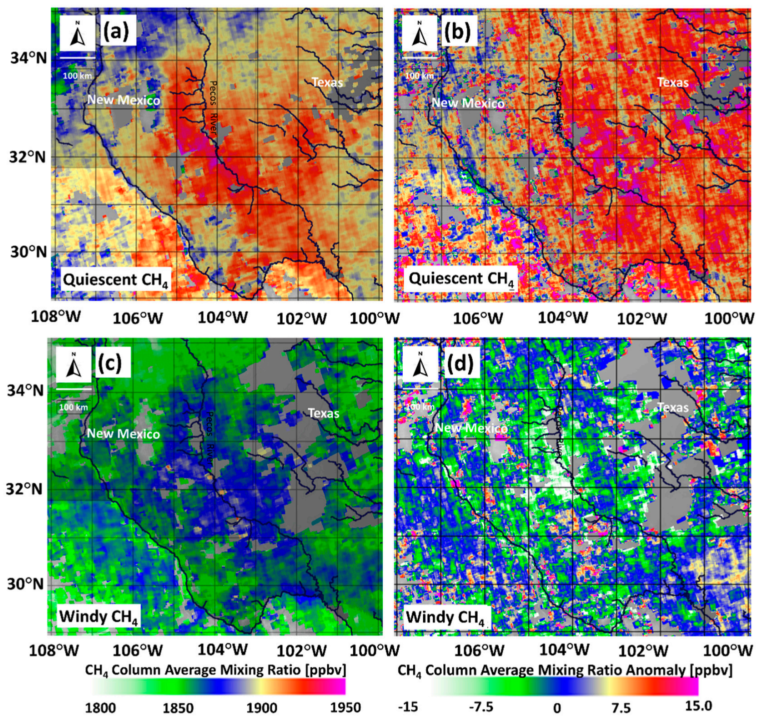

Figure 6. Average TROPOMI CH_4 column average mixing ratio (ppbv) for: (**a**) 24 September–9 October 2020 (quiescent) and (**c**) 1 April–10 May 2019 (windy); (**b**) difference (anomaly) between the "quasi-seasonal" CH_4 mean computed between 24 August and 9 November 2020 and the 24 September–9 October 2020 case study CH_4 mean; and (**d**) difference (anomaly) between the "quasi-seasonal" CH_4 mean computed between 1 March and 10 June 2019 and the 1 April–10 May 2019 case study CH_4 mean.

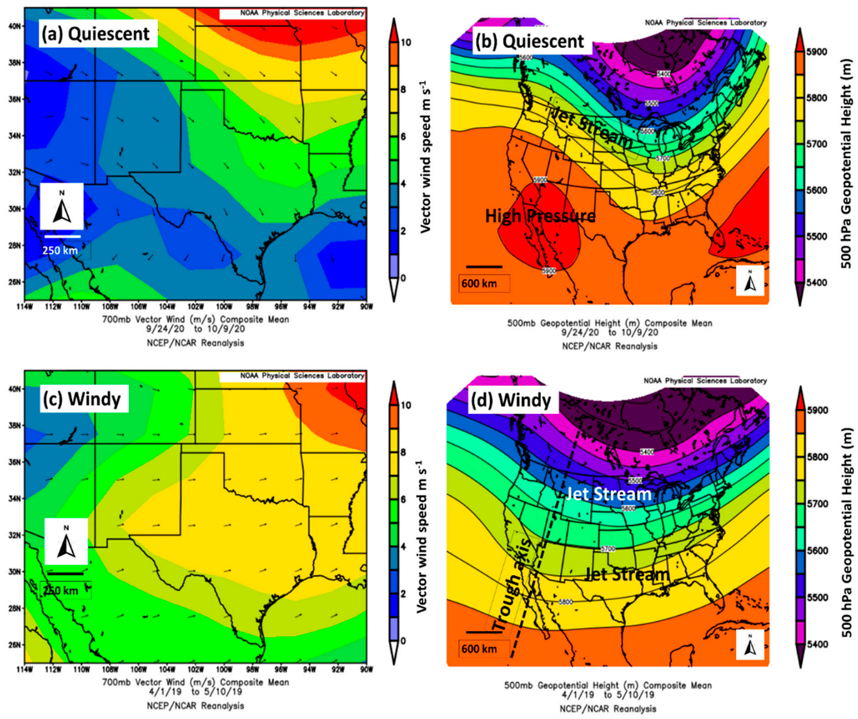

Figure 7. National Centers for Environmental Prediction (NCEP) NCEP/NCAR reanalysis of 700 hPa winds and 500 hPa geopotential heights for: (**a**) 700 hPa winds 24 September–9 October 2020 (quiescent); (**b**) 500 hPa geopotential heights from 24 September–9 October 2020 (quiescent); (**c**) 700 hPa winds 1 April–10 May 2019 (windy); and (**d**) 500 hPa geopotential heights 1 April–10 May 2019 (windy). Image composites were produced by the National Oceanic and Atmospheric Administration (NOAA) Physical Sciences Laboratory at their website https://www.psl.noaa.gov/data/composites/day/ (accessed on 14 February 2021).

The meteorological conditions across the Permian Basin during the quiescent case study period (24 September–9 October 2020) were characterized by high pressure across the western USA at 500 hPa and average 700 hPa wind speeds between 2 and 4 m s^{-1} over the Permian Basin (Figure 7a,b). These are exceptionally weak flow conditions for near mountaintop level and would result in airmass stagnation across the region. At the surface, average winds were similar to those at 700 hPa, ranging between 3.7 and 4.5 m s^{-1}, with most wind speed observations below 4 m s^{-1} at all sites observed (Figure S2). It is important to note the lack of observations of westerly wind intrusions at Dunkin and Carlsbad greater than 8 m s^{-1} during the quiescent period (Figure S2a,c). Another important feature to note at Carlsbad is the predominance of upvalley (winds flowing to the northwest) and downvalley (winds flowing to the southeast) flows. This is the wind signature of a low-level valley jet circulation that appears to be well-established during quiescent conditions in the Pecos River Valley (Figure S2a) and may contribute to the western enhancement of the Permian Basin anomaly discussed in Section 3.3.

The meteorological conditions across the Permian Basin during the windy case period (1 April–10 May 2019) were characterized by a mean trough of low pressure over the western USA at 500 hPa associated with weather systems that passed through the region during this time frame, while average 700 hPa wind speeds between 7 and 8 m s^{-1} were noted across the Permian Basin (Figure 7c,d). These wind speeds at 700 hPa are almost three times those observed during the weak flow conditions and would result in robust westerly transport of pollutants during much of this time period. At the surface, average wind speeds were also 29–35% higher than those observed during the quiescent conditions (Figure S2d–f). Of importance to note are the frequent westerly wind intrusions at Dunkin and Carlsbad greater than 8 m s^{-1} during the windy period, which would quickly scour or "mix" out nocturnal inversions that would trap pollutants and transport trace gas emissions away from the region. The occurrences of upvalley and downvalley flow patterns observed in the Pecos River Valley at Carlsbad during the windy case study period are much fewer than in the quiescent case and may illustrate the effects of the passing weather systems on disrupting the thermally-driven valley circulation (Figure S2d).

The corresponding spatial patterns in TROPOMI CH_4 observations during the two aforementioned case periods (Figure 6a,c) shows CH_4 enhancements across the entire Basin, with CH_4 column average mixing ratios ~20–40 ppbv higher than the two-year mean during the quiescent period and 10–20 ppbv lower than the two-year mean during the windy period (Figure 3). To better ascertain the impact of variations in wind speed on the CH_4 enhancements, "quasi-seasonal" (not truly seasonal, but centered on the case study time period) CH_4 averages that extended from one month before to one month after the selected case study periods were calculated for both cases (Figure 6b,d). Because there are seasonal variations in the CH_4 background, and also CH_4 variability in the Permian Basin is likely driven by other factors over time that we cannot estimate (e.g., ONG emissions, etc.), it would be inappropriate to directly quantify the differences between the windy and quiescent case periods since they are at different times of the year, have different CH_4 background values, etc. However, we can evaluate their anomalies compared to the aforementioned seasonal averages (Figure 6b,d) and potentially gain some insight into the impact of the meteorology. In both cases, the resulting anomalies (compared to the "quasi-seasonal" mean) are as expected, with the low wind case observing a positive anomaly compared to the mean quasi-seasonal value (Figure 6b) and the windy case observing a negative anomaly compared to the mean quasi-seasonal value (Figure 6d). The enhancement of the negative anomaly in the lowest portions of the Basin and just north and west of the ONG production regions in the Western Permian Basin during the windy period (insufficient retrievals were available in the windy period to observe the eastern portion of the Basin) may support the hypothesis that upvalley and upslope flows in the absence of westerly flow transport CH_4 to the north and west of the primary production regions (Figure 6d). This is discussed further in Section 3.3.

3.3. Surface Wind Climatology and Hypotheses for Western Basin CH_4 Enhancement

In this section, we discuss potential causes of the observed enhancement in CH_4 observed in TROPOMI satellite retrievals to the north and west of the primary ONG production regions (Figures 1 and 3). To do this, we analyze near surface (10-m AGL) the climatological wind roses at six stations (Figure 1) across the Permian Basin (Figure 8) between 1 December 2018 and 1 December 2020 (this time period corresponds to the TROPOMI CH_4 and NO_2 observations plotted in Figures 2 and 3), as well as the results from Section 3.2 and several parcel trajectory simulations.

Evaluation of the 10-m wind roses for the six near-surface weather stations across the Permian Basin clearly illustrates the impact of local and terrain-driven flows on the wind climatology. On the east slopes of the New Mexico and West Texas mountains, near Kent and Dunkin, the most common wind directions are southwesterly and easterly (Figure 8a,b), with easterly daytime upslope flows and nocturnal downslope flows. Northerly and southerly winds are rare at these locations. The strongest winds at these east slope stations are almost always from the southwest, associated with passing westerly disturbances, such as were frequently observed during the windy case study periods (Section 3.2). When winds are lighter, the boundary-layer flows tend to be upslope during the day (easterly) and lighter downslope (southwesterly) at night (not shown). The daytime upslope flow, combined with nocturnal inversions in the Pecos River Valley during quiescent conditions followed by daytime solar heating and mixing of the boundary-layer over and east of the Pecos River Valley, would result in the upslope transport of emissions from the ONG production regions to the east up the eastern slopes of the New Mexico and West Texas mountains.

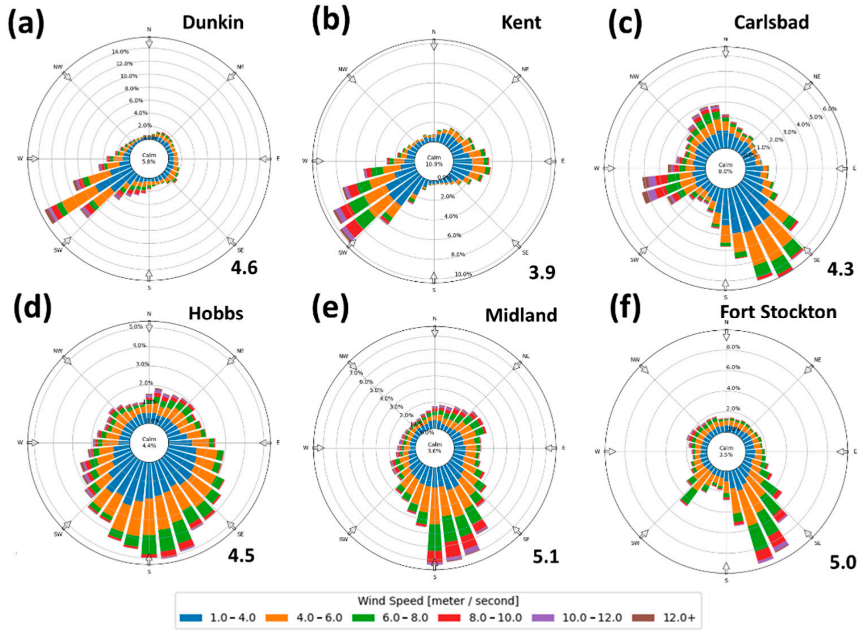

Figure 8. Ten-meter wind rose plots for the six weather stations shown in Figure 1 and listed in for the 24-month period 1 December 2018–1 December 2020: (**a**) Dunkin, New Mexico; (**b**) Kent, Texas; (**c**) Carlsbad, New Mexico; (**d**) Hobbs, New Mexico; (**e**) Midland, Texas; and (**f**) Fort Stockton, Texas. Calm wind observations are noted in the center of the wind rose, and the mean wind speed (in meters per second) at each of the six stations is shown in the lower right corner of each plot. The frequency of winds observed from each direction is shown by the location on the wind rose, while the wind speed associated with that direction is shown according to the speed color scale listed above.

While upslope or downslope winds dominate the wind climatology along the eastern slopes of the New Mexico and West Texas mountain ranges, it appears that an upvalley and downvalley wind regime occurs frequently (climatologically speaking) along the Pecos River Valley from near Pecos, Texas past Carlsbad, New Mexico toward Roswell, New Mexico. Analysis of the Carlsbad climatological wind rose clearly indicates a preponderance of southeasterly winds between 1 and 8 m s^{-1} (Figure 8) in the two-year climatology.

During quiescent weather, the combination of southerly upvalley and easterly upslope flows in this region would be expected to transport CH_4 northwestward from the high-density emissions region extending from near Fort Stockton, Texas to Carlsbad, New Mexico (see Figures 1 and 3), potentially contributing to the western expansion of the Permian Basin CH_4 anomaly (Figures 1 and 3). The New Mexico and West Texas mountains may also act as a large-scale blockage that further limits the dispersion of CH_4 during quiescent weather periods.

To further support this hypothesis of the net northwestward CH_4 transport by upvalley and slope flows, NOAA HYSPLIT model trajectories forced by 3 km HRRR model output were conducted to illustrate the combined effect of upslope and valley flows in the western portion of the Permian Basin on transporting pollution to the north and west (Figure 9) during the 24 September–9 October 2020 quiescent case. Model trajectories of particles initialized every 5 h during a 60-h period extending from 1200 UTC 30 September 2020 until 0000 UTC 3 October 2020 in the western Permian Basin are almost all transported to the north and west from the high ONG production regions (Carlsbad, New Mexico on the north end (Figure 9a) and Pecos, Texas on the south end (Figure 9b), thus supporting further the wind rose analysis that this is a favored flow trajectory for air parcels originating in the ONG production regions of the Permian Basin during times when synoptic westerly flows are not dominant.

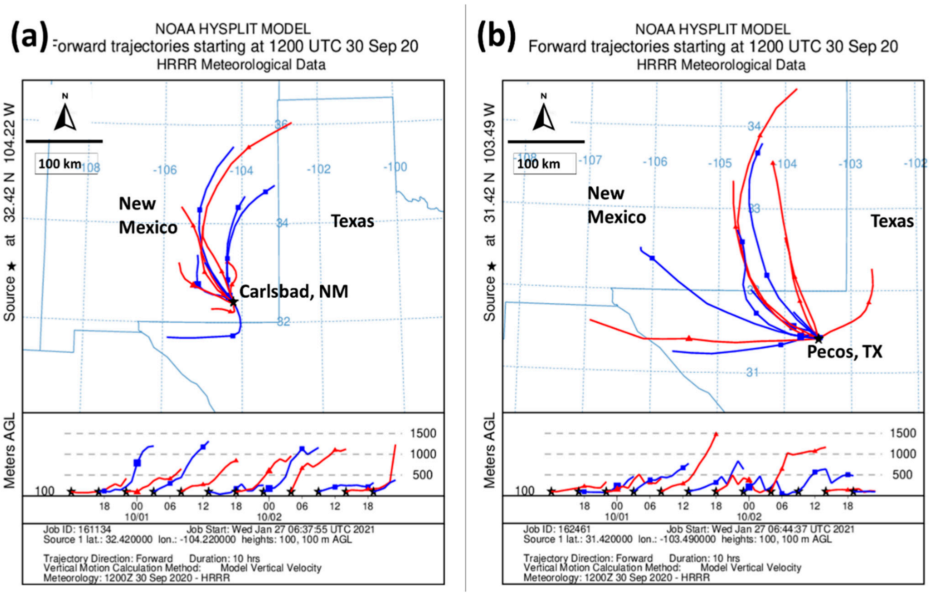

Figure 9. NOAA HYSPLITT model trajectories initialized every 5 h between 1200 UTC 30 September 2020 and 0000 UTC 3 October 2020 at: (**a**) Carlsbad, New Mexico; and (**b**) Pecos, Texas. The HRRR model was used to drive the trajectory simulations. Particles were initialized at a height of 100 m above ground level (AGL).

The hypothesis of transport of CH_4 from the ONG production regions toward the northwest in the absence of strong westerly flow appears to be supported by the quiescent case study analysis, trajectory simulations, and climatological surface wind analyses presented. Figure 10 illustrates graphically the various flows (upvalley and upslope), in addition to other factors such as strength of westerly winds and atmospheric stability that impact the spatial and temporal variability of the Permian Basin methane column enhancements.

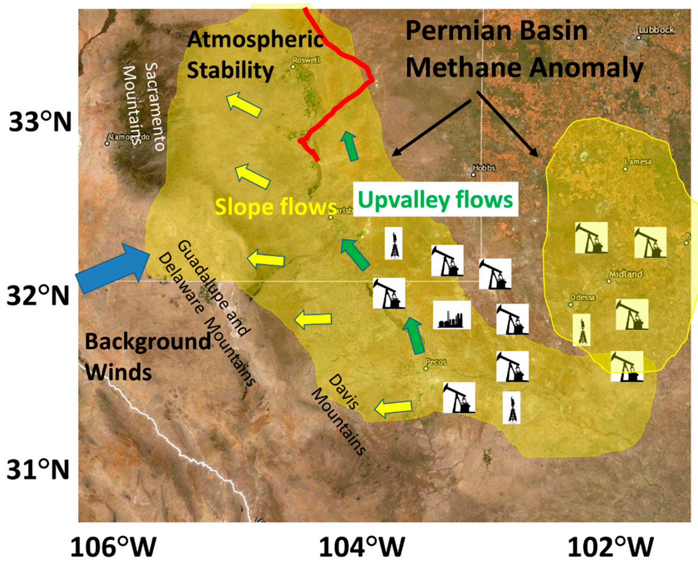

Figure 10. Schematic illustration of the Permian Basin methane anomaly region noted from TROPOMI and hypothesized meteorological drivers.

4. Discussion

While several recent studies have investigated the impacts of meteorological forcing on observed spatial variability in NO_2 (e.g., [32–37]), this is the first study to our knowledge to link CH_4 variability from TROPOMI to meteorology in an ONG production region.

As the quality and period of record of observations in TROPOMI NO_2 and CH_4 retrievals continues to increase, the ability to extract meaningful linkages between meteorological forcing and observed NO_2 and CH_4 variations across ONG regions will also continue to grow.

In this study, temporal trends from TROPOMI measurements of NO_2 and CH_4 were not evaluated due to multiple uncertainties including algorithm changes, unknown background values, spatial and temporal gaps in valid satellite retrievals, and uncorrected altitude and surface albedo CH_4 retrievals [25,46]. After careful evaluation of data availability and any temporal gap errors, temporal trends over multiple years could be potentially be evaluated after correcting for albedo and altitude effects (CH_4), while new improved cloud pressure effects for NO_2 will also be available. A recent study evaluated TROPOMI from January to June 2020 over the Permian Basin and noted that a change in cloud masks in March 2020 resulted in a decrease in available valid CH_4 retrievals [19]. Over high albedo surfaces and during cloudy periods, the frequency of satellite CH_4 observations is often limited [25].

As this study demonstrated, the lack of valid CH_4 pixels is a major limitation, and hopefully improved TROPOMI CH_4 retrieval frequency can be obtained in the future. The second windy case study period selected for this paper was extended to 40 days because the first, shorter period was found to have very limited spatial coverage of CH_4 observations. Future studies looking to determine trends from the data will need to carefully analyze the frequency and spatial coherence of the satellite retrievals. A recent study in the Permian Basin observed entire months where coverage was sparse in certain locations [19], and arial and tower measurements with gridded ONG production data between January and August 2020 were used to estimate methane fluxes in several small targeted subregions of the Basin, but a limited number of satellite estimates over their targeted regions precluded any direct comparisons between observations and TROPOMI [19]. Better determining which ONG regions and basins can be utilized for TROPOMI satellite observations, which ones have too high surface reflectance or too frequent cloud or snow cover, and which basins have ground observations to validate satellite data against will all be important considerations in the future analysis of TROPOMI CH_4 retrievals over these regions [25,69]. Using satellite data in concert with multiple in situ measurements to validate the results is also recommended as future work.

Better understanding of recent trends in production, venting, flaring, and transportation capacity is needed in the Permian Basin to combine with available TROPOMI measurements [50]. Another trace gas that deserves careful analysis over the Permian Basin is carbon monoxide (CO), as well as carbon dioxide (CO_2). Combining high resolution, accurate chemical transport models with multiple satellite trace gas retrievals simultaneously could inform emission source apportionment from ONG regions.

While there is some uncertainty in our NO_2 and CH_4 retrievals over the Permian Basin, a recent study that utilized the corrected elevation and albedo products and analyzed several months of data also noted the presence of the western extension of the Permian Basin anomaly presented in this paper [50]. The study could not "explain the methane enhancement extending outside the Delaware Basin", which has implications for model inversion and emission attribution. It is possible that the 25–30 km horizontal grid of the GEOS-Chem model used in that study was unable to properly capture the complex meteorological flows. Another additional recent short field study in 2017 in the western Permian Basin also supports the findings of this paper of upslope winds transporting light alkene VOCs from the Permian Basin towards the northwest [70]. In boundary-layer meteorology, the daytime upslope and upvalley flows are well documented [71,72], although the spatial and temporal effects of those transport processes have not been specifically identified in satellite imagery to our knowledge. Similar upslope westerly flows have also been found to be important in the ONG region east of Denver, Colorado [73].

Additional observations and trajectory modeling of the boundary-layer flows described here are needed to fully analyze the potential impacts of variable meteorology on spatial patterns in trace gases and quantify the net impact of upvalley and upslope flows on trace gas transport northwestward from the most productive regions of the Permian Basin. In this study, only near-surface (10-m AGL) wind observations were available for our analysis. The upper-level wind analyses derived from National Weather Service twice-per-day radiosondes (with wind, temperature, humidity, and pressure) at Midland, Texas are too far east to capture the complex boundary-layer meteorology associated with the mountainous terrain and Pecos River Valley to the west. In the future, studies with vertical profiling wind lidars are needed to better characterize the complex wind systems that exist across the high plains, Pecos River Valley, and eastern mountain slopes of New Mexico and West Texas. Future coupled atmospheric and chemical transport modeling studies, emission studies, and field campaigns across the region are needed to build on the analysis conducted here. We recommend that future field work bring together both boundary-layer meteorology and chemistry field and modeling expertise to provide a complete and accurate picture of the transport, emissions, and chemistry processes in the Permian Basin associated with ONG activities.

5. Conclusions

This study used meteorological observations (surface and aloft), model trajectories, and a two-year climatology (1 December 2018–1 December 2020) of TROPOMI CH_4 retrievals to investigate meteorological drivers of spatial CH_4 variability within the Permian Basin. During quiescent atmospheric conditions, low wind speeds result in greater enhancement of CH_4 within the Basin compared to windy periods, when local CH_4 emissions are more quickly transported away from the Basin. It is hypothesized that slope and valley flows may transport CH_4 northwestward toward the east slopes of the Western Texas and Eastern New Mexico Mountains, resulting in the western expansion of the Permian Basin CH_4 anomaly first noted by a recent study [50], but more research is needed to verify this hypothesis.

This study provides an example of the potential future value of utilizing satellite-derived CH_4 for atmospheric photochemical transport studies (assuming emission locations and rates are known). CH_4 from satellite has been used in previous atmospheric inversion modeling and transport studies to estimate CH_4 emissions [74–76]. The advent of high-resolution satellite data now provides new opportunities for observing from space the impacts of atmospheric flow patterns on the regional distribution of pollutants. Daily spatial satellite retrievals of CH_4, such as those now available from TROPOMI sensor, could be used in combination with emissions datasets and high-resolution modeling to better inform our understanding of CH_4 in the atmosphere.

The satellite observations presented in this study also provide motivation for field observations and modeling of the impact of the transport of primary pollutants and pollutant precursors and photochemical ozone production across the Permian Basin and regions downwind, similar to other regions [77,78]. Field studies have shown that a portion of the ozone pollution problems in along the Colorado Front Range are exacerbated by precursor emissions from ONG industry being transported by easterly winds toward the foothills of the Rocky Mountains [73], and a recent study [70] found elevated ozone and an abundance of light alkenes from oil and gas influence at Carlsbad Caverns National Park, west of the Permian Basin, which also supports the need for further coupled chemical and meteorological studies in the Permian Basin.

Supplementary Materials: The following are available online at https://www.mdpi.com/2072-4292/13/5/896/s1, Figure S1: 10-m wind rose plots for short-term quiescent (16–23 March 2019) and windy (8–15 March 2019) cases. Carlsbad (a). quiescent and (d). windy cases; Fort Stockton (b). quiescent and (e). windy cases; and Dunkin (c). quiescent and (f). windy cases. Calm wind observations are noted in the center of the wind rose, and the mean wind speed (in meters per second) at each of the 6 stations is shown in the lower right corner of each plot. The frequency of winds observed from each direction is shown by the location on the wind rose, while the wind speed associated with that direction is shown according to the speed color scale listed above. Wind roses courtesy of the Iowa State University custom wind rose feature [63], Figure S2: 10-m wind rose plots for longer term quiescent (24 September–9 October 2020) and windy (1 April–10 May 2019) cases. Carlsbad (a). quiescent and (d). windy cases; Fort Stockton (b). quiescent and (e). windy cases; and Dunkin (c). quiescent and (f). windy cases. Calm wind observations are noted in the center of the wind rose, and the mean wind speed (in meters per second) at each of the 6 stations is shown in the lower right corner of each plot. The frequency of winds observed from each direction is shown by the location on the wind rose, while the wind speed associated with that direction is shown according to the speed color scale listed above. Wind roses courtesy of the Iowa State University custom wind rose feature [63], Table S1: Description of TROPOMI Sensor Level 2 product version used (transferred from the TROPOMI readme documents available on the TROPOMI website [51] in the processing of Level 3 GEE products (Table 2) available on the GEE cloud computing platform.

Funding: A Kilgore Faculty Research grant from West Texas A&M University helped support and inspire this research. A West Texas A&M University Foundation Development grant funded the open access publication costs for this manuscript.

Institutional Review Board Statement: Not applicable.

Informed Consent Statement: Not applicable.

Data Availability Statement: Several publicly available datasets were used in this study. Satellite data from the European Space Agency (ESA) stored on the Google Earth Engine can be found here: [https://developers.google.com/earth-engine/datasets/catalog/]. Meteorological analyses can be found here: [https://www.psl.noaa.gov/data/composites/day/]. Publically available meteorological surface station data can be found at the Iowa State Mesonet: [https://mesonet.agron.iastate.edu/].

Acknowledgments: The author is extremely appreciative of the four anonymous expert reviewers whose time and effort improved this manuscript. West Texas A&M Information Technology for supporting computing capabilities for conducting research at West Texas A&M is acknowledged, including Michael Young, James Webb, and Lane Greene. The Google Earth Engine platform with associated TROPOMI satellite data processing, storage, and JavaScript code editor made this study possible. The support of graduate school personnel and other faculty and staff at West Texas A&M University on the overall research efforts, including Angela Spaulding, Teresa Clemons, and Glenda Norton, is also acknowledged. Simon Ilyushchenko from GEE is also acknowledged for his expertise in answering questions about GEE TROPOMI products.

Conflicts of Interest: The author declares no conflict of interest.

References

1. Yazdan, M.M.S.; Ahad, M.T.; Jahan, I.; Mazumder, M. Review on the Evaluation of the Impacts of Wastewater Disposal in Hydraulic Fracturing Industry in the United States. *Technologies* **2020**, *8*, 67. [CrossRef]
2. Kelly, E.N.; Schindler, D.W.; Hodson, P.V.; Short, J.W.; Radmanovich, R.; Nielsen, C.C. Oil sands development contributes elements toxic at low concentrations to the Athabasca River and its tributaries. *Proc. Natl. Acad. Sci. USA* **2010**, *107*, 16178–16183. [CrossRef]
3. Nelson, R.; Heo, J. Monitoring environmental parameters with oil and gas developments in the Permian Basin, USA. *Int. J. Environ. Res. Public Health* **2020**, *17*, 4026. [CrossRef]
4. Bruhwiler, L.M.; Basu, S.; Bergamaschi, P.; Bousquet, P.; Dlugokencky, E.; Houweling, S.; Ishizawa, M.; Kim, H.-S.; Locatelli, R.; Maksyutov, S.; et al. US CH4 emissions from oil and gas production: Have recent large increases been detected? *J. Geophys. Res.-Atmos.* **2017**, *122*, 4070–4083. [CrossRef]
5. Thompson, R.L.; Nisbet, E.G.; Pisso, I.; Stohl, A.; Blake, D.; Dlugokencky, E.J.; Helmig, D.; White, J.W.C. Variability in atmospheric methane from fossil fuel and microbial sources over the last three decades. *Geophys. Res. Lett.* **2018**, *45*, 11499–11508. [CrossRef]
6. Alvarez, R.A.; Zavala-Araiza, D.; Lyon, D.R.; Allen, D.T.; Barkley, Z.R.; Brandt, A.R.; Davis, K.J.; Herndon, S.C.; Jacob, D.J.; Karion, A.; et al. Assessment of methane emissions from the U.S. oil and gas supply chain. *Science* **2018**, *361*, 186–188. [CrossRef]
7. Garcia-Gonzales, D.; Shonkoff, S.; Hays, J.; Jerrett, M. Hazardous air pollutants associated with upstream oil and natural gas development: A critical synthesis of current peer-reviewed literature. *Annu. Rev. Public Health* **2019**, *40*, 283–304. [CrossRef]
8. Turner, A.J.; Frankenberg, C.; Kort, E.A. Interpreting contemporary trends in atmospheric methane. *Proc. Natl. Acad. Sci. USA* **2019**, *116*, 2805–2813. [CrossRef] [PubMed]
9. Kaplan, G.; Avdan, Z.Y.; Avdan, U. Spaceborne Nitrogen Dioxide Observations from the Sentinel-5P TROPOMI over Turkey. *Proceedings* **2019**, *18*, 4. [CrossRef]
10. Olstrup, H.; Johansson, C.; Forsberg, B.; Åström, C. Association between Mortality and Short-Term Exposure to Particles, Ozone and Nitrogen Dioxide in Stockholm, Sweden. *Int. J. Environ. Res. Public Health* **2019**, *16*, 1028. [CrossRef]

11. Howarth, R.W. A bridge to nowhere: Methane emissions and the greenhouse gas footprint of natural gas. *Energy Sci. Eng.* **2014**, *2*, 47–60. [CrossRef]
12. Grubert, E.A.; Brandt, A.R. Three considerations for modeling natural gas system methane emissions in the life cycle assessment. *J. Clean. Prod.* **2019**, *222*, 760–767. [CrossRef]
13. Schwietzke, S.; Pétron, G.; Conley, S.; Pickering, C.; Mielke-Maday, I.; Dlugokencky, E.J.; Tans, P.P.; Vaughn, T.; Bell, C.; Zimmerle, D.; et al. Improved Mechanistic Understanding of Natural Gas Methane Emissions from Spatially Resolved Aircraft Measurements. *Environ. Sci. Technol.* **2017**, *51*, 7286–7294. [CrossRef]
14. Foster, C.S.; Crosman, E.T.; Holland, L.; Mallia, D.V.; Fasoli, B.; Bares, R.; Horel, J.; Lin, J.C. Confirmation of elevated methane emissions in Utah's Uintah Basin with ground-based observations and a high-resolution transport model. *J. Geophys. Res.–Atmos.* **2017**, *15*, 411–419. [CrossRef]
15. Robertson, A.M.; Edie, R.; Field, R.A.; Lyon, D.; McVay, R.; Omara, M.; Zavala-Araiza, D.; Murphy, S.M. New Mexico Permian Basin measured well pad methane emissions are a factor of 5–9 times higher than U.S. EPA estimates. *Environ. Sci. Technol.* **2020**, *54*, 13926–13934. [CrossRef]
16. Barkley, Z.R.; Lauvaux, T.; Davis, K.J.; Deng, A.; Miles, N.L.; Richardson, S.J.; Cao, Y.; Sweeney, C.; Karion, A.; Smith, M.; et al. Quantifying methane emissions from natural gas production in north-eastern Pennsylvania. *Atmos. Chem. Phys.* **2017**, *17*, 13941–13966. [CrossRef]
17. Karion, A.; Sweeney, C.; Pétron, G.; Frost, G.; Hardesty, R.M.; Kofler, J.; Miller, B.R.; Newberger, T.; Wolter, S.; Banta, R.M.; et al. Methane emissions estimate from airborne measurements over a western United States natural gas field. *Geophys. Res. Lett.* **2013**, *40*, 4393–4397. [CrossRef]
18. Cardoso-Saldana, F.J.; Allen, D.T. Projecting the Temporal Evolution of Methane Emissions from Oil and Gas Production Sites. *Environ. Sci. Technol.* **2020**, *54*, 14172–14181. [CrossRef] [PubMed]
19. Lyon, D.R.; Hmiel, B.; Gautam, R.; Omara, M.; Roberts, K.; Barkley, Z.R.; David, K.J.; Miles, N.L.; Monteiro, V.C.; Richardson, S.J.; et al. Concurrent variation in oil and gas methane emissions and oil price during the COVID-19 pandemic. *Atmos. Chem. Phys. Discuss.* **2020**. [CrossRef]
20. Martin, R.V. Satellite remote sensing of air quuality. *Atmos. Environ.* **2008**, *42*, 7823–7843. [CrossRef]
21. Schneising, O.; Burrows, J.P.; Dickerson, R.R.; Buchwitz, M.; Reuter, M.; Bovensmann, H. Remote sensing of fugitive methane emissions from oil and gas production in North American tight geologic formations. *Earth's Future* **2014**, *2*, 548–558. [CrossRef]
22. Kort, E.A.; Frankenberg, C.; Costigan, K.R.; Lindenmaier, R.; Dubey, M.K.; Wunch, D. Four corners: The largest US methane anomaly viewed from space. *Geophys. Res. Lett.* **2014**, *41*, GL061503. [CrossRef]
23. Veefkind, J.; Aben, I.; McMullan, K.; Förster, H.; de Vries, J.; Otter, G.; Claas, J.; Eskes, H.; de Haan, J.; Kleipool, Q.; et al. TROPOMI on the ESA Sentinel-5 Precursor: A GMES mission for global observations of the atmospheric composition for climate, air quality and ozone layer applications. *Remote Sens. Environ.* **2012**, *120*, 7083. [CrossRef]
24. Schneising, O.; Buchwitz, M.; Reuter, M.; Vanselow, S.; Bovensmann, H.; Burrows, J.P. Remote sensing of methane leakage from natural gas and petroleum systems revisited. *Atmos. Chem. Phys.* **2020**, *20*, 9169–9182. [CrossRef]
25. De Gouw, J.A.; Veefkind, J.P.; Roosenbrand, E.; Dix, B.; Lin, J.C.; Landgraf, J.; Levelt, P.F. Daily satellite observations of methane from oil and gas production regions in the United States. *Sci. Rep.* **2020**, *10*, 1379. [CrossRef] [PubMed]
26. Cersosimo, A.; Serio, C.; Masiello, G. TROPOMI NO_2 Tropospheric Column Data: Regridding to 1 km Grid-Resolution and Assessment of their Consistency with In Situ Surface Observations. *Remote Sens.* **2020**, *12*, 2212. [CrossRef]
27. Goldberg, D.L.; Lu, Z.; Streets, D.G.; de Foy, B.; Griffin, D.; McLinden, C.A.; Lamsal, L.N.; Krotkov, N.A.; Eskes, H. Enhanced capabilities of TROPOMI NO_2: Estimating NO_x from North American cities and power plants. *Environ Sci Technol.* **2019**, *53*, 12594–12601. [CrossRef]
28. Vîrghileanu, M.; Săvulescu, I.; Mihai, B.-A.; Nistor, C.; Dobre, R. Nitrogen Dioxide (NO_2) Pollution monitoring with Sentinel-5P satellite imagery over Europe during the coronavirus pandemic outbreak. *Remote Sens.* **2020**, *12*, 3575. [CrossRef]
29. Fan, C.; Li, Y.; Guang, J.; Li, Z.; Elnashar, A.; Allam, M.; de Leeuw, G. The impact of the control measures during the COVID-19 outbreak on air pollution in China. *Remote Sens.* **2020**, *12*, 1613. [CrossRef]
30. Griffin, D.; McLinden, C.A.; Racine, J.; Moran, M.D.; Fioletov, V.; Pavlovic, R.; Mashayekhi, R.; Zhao, X.; Eskes, H. Assessing the impact of corona-virus-19 on nitrogen dioxide levels over Southern Ontario, Canada. *Remote Sens.* **2020**, *12*, 4112. [CrossRef]
31. Bauwens, M.; Compernolle, S.; Stavrakou, T.; Müller, J.-F.; van Gent, J.; Eskes, H.; Levelt, P.F.; van der, A.R.; Veefkind, J.P.; Vlietinck, J.; et al. Impact of coronavirus outbreak on NO2 pollution assessed using TROPOMI and OMI observations. *Geophys. Res. Lett.* **2020**, *47*. [CrossRef]
32. Lorente, A.; Boersma, K.F.; Eskes, H.J.; Veefkind, J.P.; Van Geffen, J.H.G.M.; De Zeeuw, M.B.; Van Der Gon, H.A.C.D.; Beirle, S.; Krol, M.C. Quantification of nitrogen oxides emissions from build-up of pollution over Paris with TROPOMI. *Sci. Rep.* **2019**, *9*, 20033. [CrossRef]
33. Solberg, S.; Walker, S.-E.; Schneider, P.; Guerreiro, C. Quantifying the Impact of the Covid-19 Lockdown Measures on Nitrogen Dioxide Levels throughout Europe. *Atmosphere* **2021**, *12*, 131. [CrossRef]
34. Zhao, X.; Griffin, D.; Fioletov, V.; McLinden, C.; Cede, A.; Tiefengraber, M.; Müller, M.; Bognar, K.; Strong, K.; Boersma, F.; et al. Assessment of the quality of TROPOMI high-spatial-resolution NO_2 data products in the Greater Toronto Area. *Atmos. Meas. Tech.* **2020**, *13*, 2131–2159. [CrossRef]

35. Goldberg, D.L.; Anenberg, S.C.; Griffin, D.; McLinden, C.A.; Lu, Z.; Streets, D.G. Disentangling the impact of the COVID-19 lockdowns on urban NO_2 from natural variability. *Geophys. Res. Lett.* **2020**, *47*. [CrossRef] [PubMed]
36. Wang, Z.; Uno, I.; Yumimoto, K.; Itahashi, S.; Chen, X.; Yang, W.; Wang, Z. Impacts of COVID-19 lockdown, spring festival and meteorology on the NO_2 variations in early 2020 over China based on in-situ observations, satellite retrievals and model simulations. *Atmos. Environ.* **2021**, *244*, 117972. [CrossRef] [PubMed]
37. Griffin, D.; Zhao, X.; McLinden, C.A.; Boersma, F.; Bourassa, A.; Dammers, E.; Degenstein, D.; Eskes, H.; Fehr, L.; Fioletov, V.; et al. High-resolution mapping of nitrogen dioxide wWith TROPOMI: First results and validation over the Canadian oil sands. *Geophys. Res. Lett.* **2019**, *46*, 1049–1060. [CrossRef]
38. Cunnold, D.M.; Steele, L.P.; Fraser, P.J.; Simmonds, P.G.; Prinn, R.G.; Weiss, R.F.; Porter, L.W.; O'Doherty, S.; Langenfelds, R.L.; Krummel, P.B.; et al. In situ measurements of atmospheric methane at GAGE/AGAGE sites during 1985–2000 and resulting source inferences. *J. Geophys. Res.* **2002**, *107*, 4225. [CrossRef]
39. Hsu, Y.-K.; VanCuren, T.; Park, S.; Jakober, C.; Herner, J.; FitzGibbon, M.; Blake, D.R.; Parrish, D.D. Methane emissions inventory verification in southern California. *Atmos. Environ.* **2010**, *44*, 1–7. [CrossRef]
40. Verhoelst, T.; Compernolle, S.; Pinardi, G.; Lambert, J.-C.; Eskes, H.J.; Eichmann, K.-U.; Fjæraa, A.M.; Granville, J.; Niemeijer, S.; Cede, A.; et al. Ground-based validation of the Copernicus Sentinel-5P TROPOMI NO_2 measurements with the NDACC ZSL-DOAS, MAX-DOAS and Pandonia global networks. *Atmos. Meas. Tech.* **2021**, *14*, 481–510. [CrossRef]
41. Dimitropoulou, E.; Hendrick, F.; Pinardi, G.; Friedrich, M.M.; Merlaud, A.; Tack, F.; De Longueville, H.; Fayt, C.; Hermans, C.; Laffineur, Q.; et al. Validation of TROPOMI tropospheric NO_2 columns using dual-scan multi-axis differential optical absorption spectroscopy (MAX-DOAS) measurements in Uccle, Brussels. *Atmos. Meas. Tech.* **2020**, *13*, 5165–5191. [CrossRef]
42. Judd, L.M.; Al-Saadi, J.A.; Szykman, J.J.; Valin, L.C.; Janz, S.J.; Kowalewski, M.G.; Eskes, H.J.; Veefkind, J.P.; Cede, A.; Mueller, M.; et al. Evaluating Sentinel-5P TROPOMI tropospheric NO_2 column densities with airborne and Pandora spectrometers near New York City and Long Island Sound. *Atmos. Meas. Tech.* **2020**, *13*, 6113–6140. [CrossRef]
43. Ialongo, I.; Virta, H.; Eskes, H.; Hovila, J.; Douros, J. Comparison of TROPOMI/Sentinel-5 Precursor NO_2 observations with ground-based measurements in Helsinki. *Atmos. Meas. Tech.* **2020**, *13*, 205–218. [CrossRef]
44. Wang, C.; Wang, T.; Wang, P.; Rakitin, V. Comparison and validation of TROPOMI and OMI NO2 observations over China. *Atmosphere* **2020**, *11*, 636. [CrossRef]
45. Cheng, L.; Tao, J.; Valks, P.; Yu, C.; Liu, S.; Wang, Y.; Xiong, X.; Wang, Z.; Chen, L. NO_2 retrieval from the environmental trace gases monitoring instrument (EMI): Preliminary results and intercomparison with OMI and TROPOMI. *Remote Sens.* **2019**, *11*, 3017. [CrossRef]
46. Lorente, A.; Borsdorff, T.; Butz, A.; Hasekamp, O.; de Brugh, J.A.; Schneider, A.; Hase, F.; Kivi, R.; Wunch, D.; Pollard, D.F.; et al. Methane retrieved from TROPOMI: Improvement of the data product and validation of the first two years of measurements. *Atmos. Meas. Tech.* **2021**, *14*, 665–684. [CrossRef]
47. Hasekamp, O.; Lorente, A.; Hu, H.; Butz, A.; de Brugh, A.A.; Landgraf, J. Algorithm theoretical baseline document for Sentinel-5 Precursor methane retrieval. Available online: https://sentinel.esa.int/documents/247904/2476257/Sentinel-5P-TROPOMI-ATBD-Methane-retrieval (accessed on 26 February 2021).
48. Yang, Y.; Zhou, M.; Langerock, B.; Sha, M.K.; Hermans, C.; Wang, T.; Ji, D.; Vigouroux, C.; Kumps, N.; Wang, G.; et al. New ground-based Fourier-transform near-infrared solar absorption measurements of XCO_2, XCH_4 and XCO at Xianghe, China. *Earth Syst. Sci. Data* **2020**, *12*, 1679–1696.
49. Schneising, O.; Buchwitz, M.; Reuter, M.; Bovensmann, H.; Burrows, J.P.; Borsdorff, T.; Deutscher, N.M.; Feist, D.G.; Griffith, D.W.T.; Hase, F.; et al. A scientific algorithm to simultaneously retrieve carbon monoxide and methane from TROPOMI onboard Sentinel-5 Precursor. *Atmos. Meas. Tech.* **2019**, *12*, 6771–6802. [CrossRef]
50. Zhang, Y.; Gautam, R.; Pandey, S.; Omara, M.; Maasakkers, J.D.; Sadavarte, P.; Lyon, D.; Nesser, H.; Sulprizio, M.P.; Varon, D.J.; et al. Quantifying methane emissions from the largest oil-producing basin in the United States from space. *Sci. Adv.* **2020**, *6*, eaaz5120. [CrossRef]
51. Tropomi Level 2 Products. Available online: www.tropomi.eu/data-products/level-2-products (accessed on 28 January 2021).
52. Van Geffen, J.H.G.M.; Eskes, H.J.; Boersma, K.F.; Maasakkers, J.D.; Veefkind, J.P. TROPOMI ATBD of the Total and Tropospheric NO2 Data Products. Available online: http://www.tropomi.eu/documents/atbd/ (accessed on 10 December 2020).
53. Gorelick, N.; Hancher, M.; Dixon, M.; Ilyushchenko, S.; Thau, D.; Moore, R. Google Earth Engine: Planetary-scale geospatial analysis for everyone. *Remote Sens. Environ.* **2017**, *202*, 18–27. [CrossRef]
54. Tamiminia, H.; Salehi, B.; Mahdianpari, M.; Quackenbush, L.; Adeli, S.; Brisco, B. Google Earth Engine for geo-big data applications: A meta-analysis and systematic review. *ISPRS J. Photogramm. Remote Sens.* **2020**, *164*, 152–170. [CrossRef]
55. Topical Collection Special Issue of Remote Sensing: "Google Earth Engine Applications". Available online: https://www.mdpi.com/journal/remotesensing/special_issues/GEE (accessed on 20 December 2020).
56. Sentinel-5P OFFL CH4. Available online: https://developers.google.com/earth-engine/datasets/catalog/COPERNICUS_S5P_OFFL_L3_CH4 (accessed on 19 December 2020).
57. Harpconvert. Available online: http://stcorp.github.io/harp/doc/html/harpconvert.html (accessed on 13 February 2021).
58. Sentinel-5P OFFL NO2. Available online: https://developers.google.com/earth-engine/datasets/catalog/COPERNICUS_S5P_OFFL_L3_NO2 (accessed on 15 December 2020).

59. Hu, H.; Hasekamp, O.; Butz, A.; Galli, A.; Landgraf, J.; de Brugh, J.A.; Borsdorff, T.; Scheepmaker, R.; Aben, I. The operational methane retrieval algorithm for TROPOMI. *Atmos. Meas. Tech.* **2016**, *9*, 5423–5440. [CrossRef]
60. Van Geffen, J.; Boersma, K.F.; Eskes, H.; Sneep, M.; Linden, M.T.; Zara, M.; Veefkind, J.P. S5P TROPOMI NO_2 slant column retrieval: Method, stability, uncertainties and comparisons with OMI. *Atmos. Meas. Tech.* **2020**, *13*, 1315–1335. [CrossRef]
61. Horel, J.; Splitt, M.; Dunn, L.; Pechmann, J.; White, B.; Ciliberti, C.; Lazarus, S.; Slemmer, J.; Zaff, D.; Burks, J. Mesowest: Cooperature Mesonets in the Western United States. *Bull. Am. Meteorol. Soc.* **2002**, *83*, 211–226. [CrossRef]
62. Mesowest. Available online: https://mesowest.utah.edu/ (accessed on 19 December 2020).
63. Iowa State Mesonet. Available online: https://mesonet.agron.iastate.edu/ (accessed on 28 January 2020).
64. NCEP/NCAR Reanalysis Composites. Available online: https://www.psl.noaa.gov/data/composites/hour/ (accessed on 30 January 2021).
65. Draxler, R.R.; Rolph. HYSPLIT (Hybrid Single-Particle Lagrangian Integrated Trajectory) model access via NOAA ARL READY Website. Available online: http://www.arl.noaa.gov/ready/hysplit4.html (accessed on 28 January 2021).
66. Stein, A.F.; Draxler, R.R.; Rolph, G.D.; Stunder, B.J.B.; Cohen, M.D.; Ngan, F. NOAA's HYSPLIT Atmospheric Transport and Dispersion Modeling System. *Bull. Am. Meteorol. Soc.* **2015**, *96*, 2059–2077. [CrossRef]
67. Benjamin, S.G.; Weygandt, S.S.; Brown, J.M.; Hu, M.; Alexander, C.R.; Smirnova, T.G.; Olson, J.B.; James, E.P.; Dowell, D.C.; Grell, G.A.; et al. A North American hourly assimilation and model forecast cycle: The rapid refresh. *Mon. Weather Rev.* **2016**, *144*, 1669–1694. [CrossRef]
68. He, T.; Gao, F.; Liang, S.; Peng, Y. Mapping Climatological Bare Soil Albedos over the Contiguous United States Using MODIS Data. *Remote Sens.* **2019**, *11*, 666. [CrossRef]
69. Foster, C.S.; Crosman, E.T.; Horel, J.D.; Lyman, S.N.; Fasoli, B.; Bares, R.; Lin, J.C. Quantifying methane emissions in the Uintah Basin during wintertime stagnation episodes. *Elem. Sci. Anthr.* **2019**, *7*, 24. [CrossRef]
70. Benedict, K.B.; Prenni, A.J.; El-Sayed, M.M.H.; Hecobian, A.; Zhou, Y.; Gebhart, K.A.; Sive, B.C.; Schichtel, B.A.; Collett, J.L. Volatile organic compounds and ozone at four national parks in the southwestern United States. *Atmos. Environ.* **2020**, *239*, 117783. [CrossRef]
71. De Wekker, S.F.J.; Kossmann, M.; Knievel, J.C.; Giovannini, L.; Gutmann, E.D.; Zardi, D. Meteorological Applications Benefiting from an Improved Understanding of Atmospheric Exchange Processes over Mountains. *Atmosphere* **2018**, *9*, 371. [CrossRef]
72. Miao, Y.; Liu, S.; Sheng, L.; Huang, S.; Li, J. Influence of Boundary Layer Structure and Low-Level Jet on $PM_{2.5}$ Pollution in Beijing: A Case Study. *Int. J. Environ. Res. Public Health* **2019**, *16*, 616. [CrossRef] [PubMed]
73. Evans, J.M.; Helmig, D. Investigation of the influence of transport from oil and natural gas regions on elevated ozone levels in the northern Colorado front range. *J. Air Waste Manag. Assoc.* **2017**, *67*, 196–211. [CrossRef] [PubMed]
74. Janardanan, R.; Maksyutov, S.; Tsuruta, A.; Wang, F.; Tiwari, Y.K.; Valsala, V.; Ito, A.; Yoshida, Y.; Kaiser, J.W.; Janssens-Maenhout, G.; et al. Country-Scale Analysis of Methane Emissions with a High-Resolution Inverse Model Using GOSAT and Surface Observations. *Remote Sens.* **2020**, *12*, 375. [CrossRef]
75. Kuze, A.; Kikuchi, N.; Kataoka, F.; Suto, H.; Shiomi, K.; Kondo, Y. Detection of Methane Emission from a Local Source Using GOSAT Target Observations. *Remote Sens.* **2020**, *12*, 267. [CrossRef]
76. Ayasse, A.K.; Dennison, P.E.; Foote, M.; Thorpe, A.K.; Joshi, S.; Green, R.O.; Duren, R.M.; Thompson, D.R.; Roberts, D.A. Methane Mapping with Future Satellite Imaging Spectrometers. *Remote Sens.* **2019**, *11*, 3054. [CrossRef]
77. Tian, J.; Fang, C.; Qiu, J.; Wang, J. Analysis of Pollution Characteristics and Influencing Factors of Main Pollutants in the Atmosphere of Shenyang City. *Atmosphere* **2020**, *11*, 766. [CrossRef]
78. He, J.; Lu, S.; Yu, Y.; Gong, S.; Zhao, S.; Zhou, C. Numerical Simulation Study of Winter Pollutant Transport Characteristics over Lanzhou City, Northwest China. *Atmosphere* **2018**, *9*, 382. [CrossRef]